

# (2S)-2-(3-(1-Carboxy-5-(4-<sup>211</sup>At-Astatobenzamido)Pentyl)Ureido)-Pentanedioic Acid for PSMA-Targeted $\alpha$ -Particle Radiopharmaceutical Therapy

Ana P. Kiess\*<sup>1</sup>, Il Minn\*<sup>2</sup>, Ganesan Vaidyanathan<sup>3</sup>, Robert F. Hobbs<sup>1</sup>, Anders Josefsson<sup>2</sup>, Colette Shen<sup>1</sup>, Mary Brummet<sup>2</sup>, Ying Chen<sup>2</sup>, Jaeyeon Choi<sup>3</sup>, Eftychia Koumariou<sup>3</sup>, Kwamena Baidoo<sup>4</sup>, Martin W. Brechbiel<sup>4</sup>, Ronnie C. Mease<sup>2</sup>, George Sgouros<sup>1,2</sup>, Michael R. Zalutsky<sup>3</sup>, and Martin G. Pomper<sup>1,2</sup>

<sup>1</sup>Department of Radiation Oncology and Molecular Radiation Sciences, Johns Hopkins University School of Medicine, Baltimore, Maryland; <sup>2</sup>Russell H. Morgan Department of Radiology and Radiological Science, Johns Hopkins University School of Medicine, Baltimore, Maryland; <sup>3</sup>Department of Radiology, Duke University Medical Center, Durham, North Carolina; and <sup>4</sup>Center for Cancer Research, National Cancer Institute, Bethesda, Maryland

Alpha-particle emitters have a high linear energy transfer and short range, offering the potential for treating micrometastases while sparing normal tissues. We developed a urea-based, <sup>211</sup>At-labeled small molecule targeting prostate-specific membrane antigen (PSMA) for the treatment of micrometastases due to prostate cancer (PC). **Methods:** PSMA-targeted (2S)-2-(3-(1-carboxy-5-(4-<sup>211</sup>At-astatobenzamido)pentyl)ureido)-pentanedioic acid (<sup>211</sup>At-6) was synthesized. Cellular uptake and clonogenic survival were tested in PSMA-positive (PSMA+) PC3 PIP and PSMA-negative (PSMA-) PC3 flu human PC cells after <sup>211</sup>At-6 treatment. The antitumor efficacy of <sup>211</sup>At-6 was evaluated in mice bearing PSMA+ PC3 PIP and PSMA- PC3 flu flank xenografts at a 740-kBq dose and in mice bearing PSMA+, luciferase-expressing PC3-ML micrometastases. Biodistribution was determined in mice bearing PSMA+ PC3 PIP and PSMA- PC3 flu flank xenografts. Suborgan distribution was evaluated using  $\alpha$ -camera images, and microscale dosimetry was modeled. Long-term toxicity was assessed in mice for 12 mo. **Results:** <sup>211</sup>At-6 treatment resulted in PSMA-specific cellular uptake and decreased clonogenic survival in PSMA+ PC3 PIP cells and caused significant tumor growth delay in PSMA+ PC3 PIP flank tumors. Significantly improved survival was achieved in the newly developed PSMA+ micrometastatic PC model. Biodistribution showed uptake of <sup>211</sup>At-6 in PSMA+ PC3 PIP tumors and in kidneys. Microscale kidney dosimetry based on  $\alpha$ -camera images and a nephron model revealed hot spots in the proximal renal tubules. Long-term toxicity studies confirmed that the dose-limiting toxicity was late radiation nephropathy. **Conclusion:** PSMA-targeted <sup>211</sup>At-6  $\alpha$ -particle radiotherapy yielded significantly improved survival in mice bearing PC micrometastases after systemic administration. <sup>211</sup>At-6 also showed uptake in renal proximal tubules resulting in late nephrotoxicity, highlighting the importance of long-term toxicity studies and microscale dosimetry.

**Key Words:** oncology; GU; radionuclide therapy; radiopharmaceuticals; alpha emitter; astatine; prostate cancer; prostate-specific membrane antigen; radiation dosimetry

**J Nucl Med 2016; 57:1569–1575**  
DOI: 10.2967/jnumed.116.174300

A significant fraction of men with prostate cancer (PC) develop metastatic disease with attendant consequences (1,2). For example, metastatic bone disease carries a 40% 1-y survival rate. An important group of patients to address with targeted radiopharmaceutical therapy (RPT) are those with biochemical recurrence and no imaging findings, namely, micrometastatic disease. Some of those patients will have stable disease on hormonal therapy for years but many will progress to castration-resistant prostate cancer (CRPC), with limited treatment options. Systemic agents including docetaxel, enzalutamide, and abiraterone have provided small survival benefits (3,4). The recent phase III ALSYMPCA trial of Xofigo (<sup>223</sup>RaCl<sub>2</sub>; Bayer HealthCare Pharmaceuticals) demonstrated the feasibility of  $\alpha$ -emitter RPT in CRPC (5). However, survival benefit was only 3 mo, and therapeutic effect was limited to bone metastases. To expand beyond the success of Xofigo, we developed <sup>211</sup>At-6, a urea-based  $\alpha$ -emitter that targets prostate-specific membrane antigen (PSMA), which is overexpressed more than 1,000-fold relative to normal prostate in nearly all PC and is present in solid tumor neovasculature (6–8). On the basis of clinical studies with PSMA-targeted imaging agents (9,10), both bone and soft-tissue metastases should be treatable by targeting PSMA. Moreover, the perinuclear localization of PSMA enhances tumor cell kill (11).

PSMA-targeted RPT has been confined to  $\beta^-$ -emitters including clinical studies with <sup>131</sup>I-MIP1466 (12) and <sup>177</sup>Lu-labeled J591, which was dose-limited by myelosuppression, particularly thrombocytopenia (13).  $\alpha$ -particles have clear advantages over  $\beta^-$ -particles for the treatment of micrometastases, including a high linear energy transfer and a short tissue range (14), which should facilitate selective eradication of small clusters of malignant cells while sparing surrounding normal tissue. In addition to the ALSYMPCA trial for CRPC,  $\alpha$ -particle emitters have been investigated in other clinical trials and have consistently shown only mild toxicities (15). Among

Received Feb. 17, 2016; revision accepted Apr. 11, 2016.  
For correspondence or reprints contact: Martin G. Pomper, Johns Hopkins Medical School, 1550 Orleans St., 492 CRB II, Baltimore, MD 21287.  
E-mail: mpomper@jhmi.edu  
\*Contributed equally to this work.  
Published online May 26, 2016.  
COPYRIGHT © 2016 by the Society of Nuclear Medicine and Molecular Imaging, Inc.

the  $\alpha$ -emitters,  $^{211}\text{At}$  has particularly favorable characteristics for clinical development including a 7.2-h half-life that is well matched to small-molecule therapeutics (16). A detailed review (17) summarizes the current status of  $^{211}\text{At}$ -labeled radiotherapeutics and the importance for understanding the microscale distribution of  $\alpha$ -emitters to predict toxicity and efficacy, an essential aspect of our studies.

## MATERIALS AND METHODS

### Chemistry

Compounds **1** and **2** (Fig. 1) were prepared by the method of Chen et al. and Maresca et al., respectively (18,19). Stannane **3** was prepared as previously described (18). Details regarding the synthesis of **4** and radiochemistry are presented in the supplemental materials (available at <http://jnm.snmjournals.org>).

### In Vivo Studies

**Cell Lines and Culture Conditions.** The isogenic human PC3 cell lines PIP (PSMA-positive [PSMA+]) and flu (PSMA-negative [PSMA-]) were originally obtained from Dr. Warren Heston (Cleveland Clinic) and were maintained as described (20). The androgen-independent PC3 cell line was originally derived from a human CRPC bone metastasis. The PSMA+ PC3 PIP line was stably transfected to overexpress PSMA. Parental PC3-ML-Luc cells were obtained from Dr. Mauricio Reginato (Drexel University).

**Paired-Label Uptake of  $^{131}\text{I}$ -5 and  $^{211}\text{At}$ -6.** Both PSMA+ PC3 PIP and PSMA- PC3 flu cells were plated at a density of  $5 \times 10^5$  cells/well and incubated overnight. Cells were then incubated in solutions of  $^{131}\text{I}$ -5 and  $^{211}\text{At}$ -6 in medium ( $\sim 3.7$  kBq/100  $\mu\text{L}$ ) at  $37^\circ\text{C}$  for 0.5, 1, 2, and 4 h. Cell culture supernatants were then removed, and cells were washed twice with phosphate-buffered saline. Cells were solubilized by incubation with 1 M NaOH ( $2 \times 2$  mL) for 10 min. Aliquots (100  $\mu\text{L}$ ) of cell culture supernatants, solubilized cells, and input dose standards were counted for  $^{131}\text{I}$  and  $^{211}\text{At}$  activity in an LKB Wallac 1282  $\gamma$ -counter (Perkin-Elmer), and cell-associated radioactivity as percentage of input dose was calculated. In a parallel assay, PSMA+ PC3 PIP cells were coincubated with the 2 radiotracers and (*R,S*)-2-(phosphonomethyl)pentanedioic acid (2-PMPA; 100  $\mu\text{M}$  final concentration) (21).

**In Vitro Cytotoxicity.** PSMA+ PC3 PIP cells were incubated in triplicate flasks at a density of  $5 \times 10^3$  cells at  $37^\circ\text{C}$  for 3 d. Cells were replenished with fresh medium (control) or varying concentrations of  $^{211}\text{At}$ -astatide or  $^{211}\text{At}$ -6 and incubated at  $37^\circ\text{C}$ . After 10 d, the cells were washed with phosphate-buffered saline, fixed for 5 min with 95% ethanol, stained with 0.4% trypan blue, and washed again with phosphate-buffered saline. Colonies were counted using a Darkfield Quebec Colony Counter (Cambridge Instruments). The  $\text{D}_{50}$

(dose to reduce survival to 37% on the exponential portion of the curve) and 90% confidence limits of the regression fit were determined using Sigma Plot (Jandel Scientific).

### In Vivo Studies

**Paired-Label Biodistribution of  $^{131}\text{I}$ -5 and  $^{211}\text{At}$ -6.** All animal experiments were performed following the guidelines established by the Duke and Johns Hopkins University Institutional Animal Care and Use Committees. Six- to 8-wk-old athymic mice weighing approximately 25 g (Charles River) were injected with  $10^6$  PSMA+ PC3 PIP cells into one flank and  $10^6$  PSMA- PC3 flu cells into the opposite flank. Biodistribution studies were conducted when the xenografts were 300–500  $\text{mm}^3$  in size. Mice received 0.2 MBq of each radio-tracer via the tail vein, and groups of 5 mice were sacrificed 0.5, 1, 2, 4, and 18 h after injection. Tissues were isolated, weighed, and counted for  $^{131}\text{I}$  and  $^{211}\text{At}$ . Percentages of injected dose per organ and per gram of tissue were computed. Differences in tissue uptake between the 2 radiotracers were calculated using a 2-tailed, paired Student *t* test.

**Antitumor Efficacy in Flank Xenograft Model.** Cells were grown to 80%–90% confluence before trypsinization and formulation in RPMI for inoculation. Male athymic mice weighing approximately 20 g were injected subcutaneously within the flank with  $1 \times 10^6$  PSMA+ PC3 PIP or PSMA- PC3 flu cells. Treatments were administered 7–12 d later when tumor volume was less than 200  $\text{mm}^3$ . Animals ( $n = 9$ –11 per group) received 740 kBq of  $^{211}\text{At}$ -6 intravenously or were untreated. Tumors were then measured 2–3 times per week until they reached  $10\times$  the pretreatment volume. The probability of reaching  $10\times$  initial tumor volume was characterized using Kaplan–Meier curves, and comparison was performed using the log-rank test (GraphPad Prism).

**Antitumor Efficacy in Micrometastatic Model.** To generate a PSMA-expressing metastatic PC model, PC3-ML-Luc cells (22) were infected with lentiviral particles as described (23). After infection, cells were stained with YC-36, a PSMA-targeted small molecule conjugated with fluorescein isothiocyanate (11). PSMA+ single cells were sorted using the MoFlo (DakoCytomation), and clones were established. The metastatic potential of each clone was tested by monitoring the development of metastases and progression by in vivo bioluminescence imaging (IVIS Spectrum; Perkin-Elmer) after intravenous injection of  $1 \times 10^6$  cells. Four- to 6-wk-old NOG (NOD/Shi-*scid*/IL-2R $\gamma^{\text{null}}$ ) mice (Animal Resources Core, Johns Hopkins) were injected with  $1 \times 10^6$  PC3-ML-Luc-PSMA cells. One day later, mice ( $n = 5$ /group) were injected intravenously with 37, 111, 185, or 370 kBq of  $^{211}\text{At}$ -6. Metastatic tumor progression was monitored by in vivo bioluminescence imaging and survival.

**Toxicity and Maximum Tolerated Dose.** The maximum tolerated dose was defined as the highest dose at which no animal died or lost more than 20% of its pretreatment weight. Non-tumor-bearing CD1

mice (Charles River,  $n = 10$ /group) weighing 25–30 g received intravenous injections of 0, 37, 111, 370, 740, or 1,480 kBq of  $^{211}\text{At}$ -6 and then were weighed and inspected twice per week for at least 12 mo. Urinalysis was performed monthly for each animal. On sacrifice, animals were evaluated by the Johns Hopkins Department of Comparative Pathology with serum metabolic panel, blood counts, and full necropsy including detailed histopathology of kidneys.

**$^{211}\text{At}$ -6 Tumor and Kidney Biodistribution for Dosimetry.** Male athymic mice weighing approximately 20 g were injected subcutaneously in the right and left flank areas with  $10^6$  PSMA+ PC3 PIP and  $10^6$  PSMA- PC3 flu

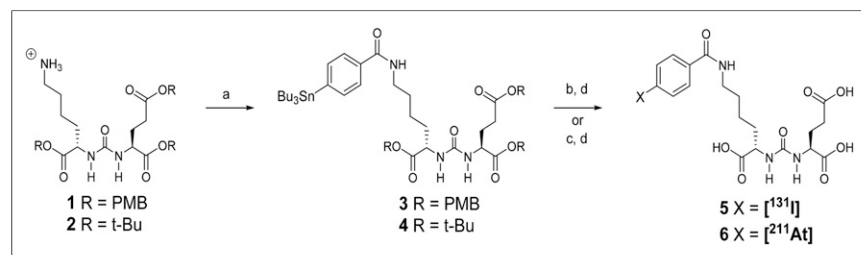


**FIGURE 1.** Synthesis of  $^{131}\text{I}$ -5 and  $^{211}\text{At}$ -6. (A) *N*-succinimidyl-4-tributylstannyl benzoate, triethylamine, methylene chloride. (B)  $^{211}\text{At}$ , *N*-chlorosuccinimide, acetic acid, methanol, room temp 30 min. (C) Na [ $^{131}\text{I}$ ]*N*-chlorosuccinimide, acetic acid, methanol, room temp 30 min. (D) Trifluoroacetic acid/water  $50^\circ\text{C}$  30 min or room temperature 60–90 min. PMB = para-methoxybenzyl.

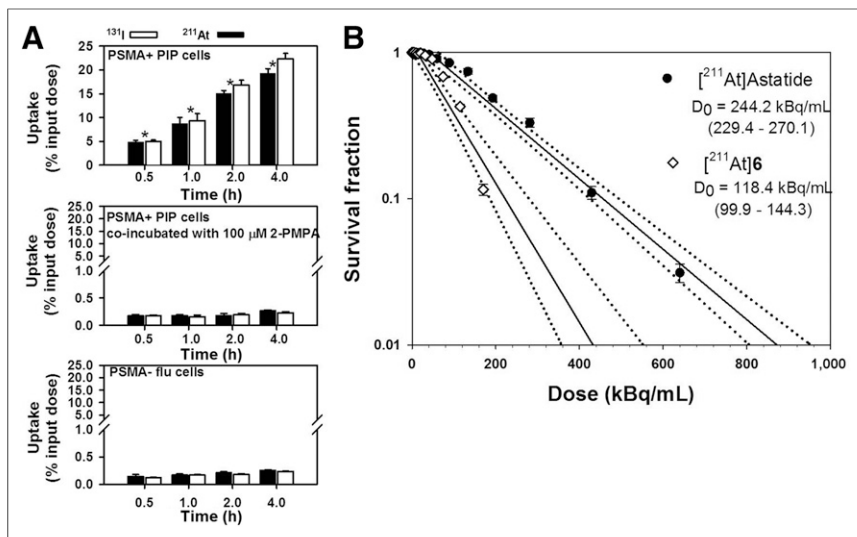


**FIGURE 2.** (A) Paired-label uptake of  $^{131}\text{I}$ -**5** and  $^{211}\text{At}$ -**6** in PSMA+ PC3 PIP and PSMA- PC3 flu cells. Uptake in PSMA+ cells also was determined in presence of PSMA inhibitor, 2-PMPA. Values indicate mean  $\pm$  SD. Asterisks indicate difference between radiotracers using paired  $t$  test ( $P < 0.05$ ). (B) Clonogenic survival of PSMA+ cells after incubation with  $^{211}\text{At}$ -astatide and  $^{211}\text{At}$ -**6**. Dashed line indicates 95% confidence limit for regression fit.

cells, respectively. Eight mice were injected intravenously with 3.7 MBq of  $^{211}\text{At}$ -**6** and sacrificed at 1 ( $n = 3$ ), 4 ( $n = 3$ ), 8 ( $n = 1$ ), and 16 h ( $n = 1$ ). The left kidney and both tumors were harvested and weighed, and activity was measured using a 1282 Compugamma  $\gamma$ -counter (Pharmacia).

**$\alpha$ -Camera Imaging.** Digital autoradiography imaging was performed using the  $\alpha$ -camera (24) to determine the activity concentration and distribution of  $^{211}\text{At}$ -**6** at subtissue levels. Kidney and tumors were frozen in dry ice and cryostat-sectioned in 8- $\mu\text{m}$  sections. Consecutive sections were taken for hematoxylin and eosin staining and  $\alpha$ -camera imaging for 15–20 min. The  $\alpha$ -camera imaging samples were also measured in the  $\gamma$ -counter to allow image quantification. Regions of interest were drawn using ImageJ Fiji (version 1.49 g; National Institutes of Health) to measure activity levels within the different compartments. In addition, the relative  $^{211}\text{At}$ -**6** activity concentrations in the subtissue level versus the average of the whole tissue sample was calculated.

**Dosimetry.** Whole-body and small-scale kidney/tumor dosimetry for  $^{211}\text{At}$ -**6** was derived from the biodistribution data and quantified  $\alpha$ -camera images, respectively. Details regarding whole-body dosimetry are provided in the supplemental data. For small-scale kidney dosimetry, histologically verified regions of interest corresponding to proximal tubules and glomeruli were drawn on  $\alpha$ -camera images and integrated over time to obtain the total number of decays. Micro-scale  $S$  values for  $^{211}\text{At}$  decays in these regions were multiplied by the total number of decays to yield the absorbed doses to proximal tubules and glomeruli. The  $S$  values were calculated according to a previously created Monte Carlo-based kidney nephron model (25).

Small-scale tumor dosimetry was done by obtaining histograms of activity uptake per time point with a same number of bins, ranking the bins by uptake and integrating over bins with the same ranking from time point to time point to obtain a time-integrated activity histogram. Absorbed fractions for self-dose and neighbor-dose for pixels (voxels) were calculated using GEANT4 Monte Carlo simulation. Activity in adjacent bins was randomly determined for each bin and the  $S$  values applied to obtain a normalized dose volume histogram.

## RESULTS

### Radiochemistry

$^{131}\text{I}$ -**5** was synthesized in radiochemical yields similar to those obtained with  $^{125}\text{I}$  (18). Astatodestannylation and in situ deprotection of **3** or **4** (Fig. 1) delivered  $^{211}\text{At}$ -**6** in  $62.6\% \pm 9.5\%$  ( $n = 23$ ) radiochemical yield using **3** in greater than 98% radiochemical purity as determined by high-performance liquid chromatography. Coinjection with nonradioactive **5** (iodinated) showed that both eluted with the same retention time on high-performance liquid chromatography. No coeluting carrier peak was observed on high-performance liquid chromatography with  $^{211}\text{At}$ -**6**.

### In Vitro Studies

The percentage uptake in PSMA+ PC3 PIP cells increased from  $5.0 \pm 0.3$  ( $^{131}\text{I}$ ) and  $4.9 \pm 0.3$  ( $^{211}\text{At}$ ) at 0.5 h to  $22.4 \pm 1.1$  ( $^{131}\text{I}$ ) and  $19.3 \pm 1.0$  ( $^{211}\text{At}$ ) at 4 h (Fig. 2A, top). The uptake of  $^{211}\text{At}$ -**6** was lower than  $^{131}\text{I}$ -**5**. PSMA specificity of uptake was demonstrated by its reduction to less

than 2% of input dose when coincubated with the PSMA inhibitor 2-PMPA (Fig. 2A, middle) (21). Moreover, uptake in PSMA- PC3 flu cells was significantly lower than in PSMA+ PC3 PIP cells (Fig. 2A, bottom). The clonogenic survival of PSMA+ PC3 PIP cells after incubation with  $^{211}\text{At}$ -astatide and  $^{211}\text{At}$ -**6** for 4 h is shown in Figure 2B. A  $D_0$  of 118.4 kBq/mL was obtained for  $^{211}\text{At}$ -**6** compared with 244.2 kBq/mL for  $^{211}\text{At}$ -astatide.

### In Vivo Studies

**Biodistribution.** Uptake of  $^{131}\text{I}$  and  $^{211}\text{At}$  in PSMA+ PC3 PIP and PSMA- PC3 flu tumors after injection of  $^{131}\text{I}$ -**5** and  $^{211}\text{At}$ -**6** is presented in Figure 3. Paired-label studies are of value because both tracers are subjected to identical conditions so that each experiment has its own control (26,27). In addition, in the case of  $^{211}\text{At}$ -labeled compounds, in vivo stability is a major concern and the paired-label biodistribution studies can shed some light on the potential effects of lower carbon-halogen bond strength on biodistribution (28). As seen in cell culture, tumor uptake increased for both agents with time and was higher for  $^{131}\text{I}$ -**5**. Except at 18 h, the difference in the uptake between the 2 radiotracers was significant. Maximum tumor uptake of  $41.5 \pm 18.4$  %ID/g for  $^{131}\text{I}$ -**5** and  $31.1 \pm 9.8$  %ID/g for  $^{211}\text{At}$ -**6** was seen at 18 h. With both radiotracers, uptake was significantly lower in PSMA- PC3 flu xenografts.

Uptake of  $^{131}\text{I}$  and  $^{211}\text{At}$  in normal tissues is given in Supplemental Tables 1 and 2, respectively. Uptake in the kidneys was high for both radiotracers. However, the renal uptake of  $^{211}\text{At}$  was only 50%–70% of that observed for  $^{131}\text{I}$  at all time points. The uptake from  $^{211}\text{At}$ -**6** in the thyroid, lungs, and stomach was higher than that from  $^{131}\text{I}$ -**5**, suggesting a higher degree of dehalogenation for  $^{211}\text{At}$ -**6**. PSMA+ PC3 PIP tumor-to-normal-tissue ratios generally increased with time (Fig. 4). Except for in the spleen and kidneys, the tumor-to-tissue ratio was higher for  $^{131}\text{I}$ -**5**.

**Antitumor Efficacy.** Nude mice bearing PSMA+ PC3 PIP flank tumors had significant tumor growth delay after treatment with 740 kBq of  $^{211}\text{At}$ -**6** compared with other groups (Fig. 5). Tumors from

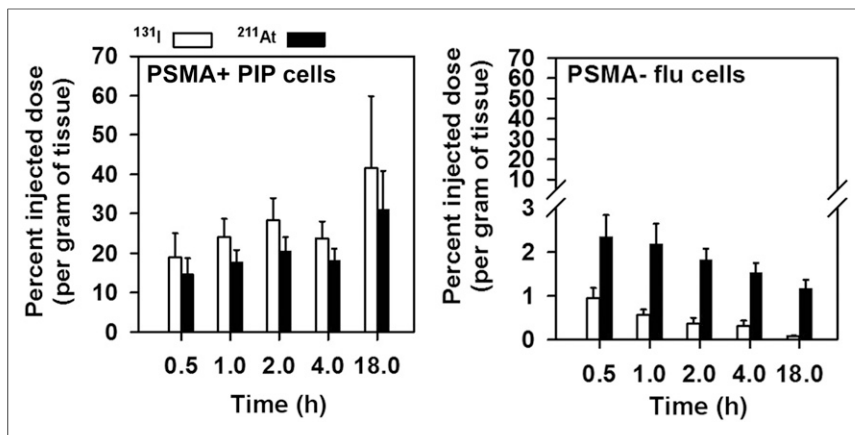


**FIGURE 3.** Uptake of  $^{131}\text{I}$  and  $^{211}\text{At}$  in PSMA+ PC3 PIP and PSMA- PC3 flu xenografts after administration of 0.2 MBq of  $^{131}\text{I}$ -5 and  $^{211}\text{At}$ -6 in athymic mice. Values indicate mean  $\pm$  SD.

2 of 11 treated animals harboring PSMA+ PC3 PIP xenografts disappeared and did not recur during the 8-mo study. Median times to reach 10 $\times$  the tumor volume for PSMA+ PC3 PIP (treated), PSMA+ PC3 PIP (untreated), PSMA- PC3 flu (treated), and PSMA- PC3 flu (untreated) were 35, 19, 24, and 19 d, respectively. The difference among treatment groups was statistically significant ( $P = 0.01$ ) by the log-rank test. Individual animal tumor volume plots are shown in Supplemental Figure 1.

**Antitumor Efficacy in Micrometastatic Model.** NOG mice injected with PC3-ML-Luc-PSMA developed metastases within the liver, kidneys, and bone (Supplemental Fig. 2). Untreated animals died within 7–8 wk after receiving cells. Median survival was 58, 59, 72, 97, and 110 d for those untreated and those receiving 37, 111, 185, and 370 kBq, respectively (Fig. 6; Supplemental Fig. 3). Survival rates were statistically different among groups ( $P < 0.0001$ ).

**In Vivo Toxicity and Maximum Tolerated Dose.** The maximum tolerated single dose of  $^{211}\text{At}$ -6 in immunocompetent CD1 mice was 37 kBq. The dose-limiting toxicity was late radiation nephropathy.

On histopathology, there was subcortical atrophy with prominent degenerative loss of the proximal tubules, tubular ectasia, and proteinosis (Fig. 7). No animals died of acute or chronic hematologic toxicity, but average hemoglobin at necropsy was 7.8 g/dL (normal, 15.4–17.2 g/dL), likely reflecting anemia due to reduced erythropoietin from nephropathy.

**$^{211}\text{At}$ -6 Tumor and Kidney Biodistribution for Dosimetry.**  $^{211}\text{At}$ -6 biodistribution for kidneys, PSMA+ PC3 PIP, and PSMA- PC3 flu tumors after a 3.7 MBq dose are shown in Supplemental Figure 5. The highest kidney uptake of  $^{211}\text{At}$ -6 occurred at 4 h ( $97.8 \pm 12.2$  %ID/g) whereas the highest uptake in PSMA+ PC3 PIP tumors occurred at 16 h ( $28.2$  %ID/g). For the PSMA- PC3 flu tumors, maximum uptake was at 1 h ( $2.1 \pm 1.4$  %ID/g).

**$\alpha$ -Camera Imaging.** More than 91% of the activity in the kidneys was localized to the cortex at all time points (Fig. 8). Hot spots were histologically verified to correspond to the proximal tubules and had activity concentrations 3.5–4.5 times higher than the entire kidney section average. In PSMA+ tumors, there were heterogeneous hot spots of activity measuring 3.8, 3.0, 2.5, and 2.5 times higher than the entire tumor section average at 1, 4, 8, and 16 h, respectively, suggesting transition toward a more homogeneous tumor distribution with time.

**Dosimetry.** Whole-organ kidney/tumor dosimetry for  $^{211}\text{At}$ -6 was based on the biodistribution data shown in Supplemental Figure 5. Considering only the  $\alpha$ -emissions and assuming local deposition within the kidney and tumors, the mean absorbed dose of  $^{211}\text{At}$ -6 was 24.6, 10.0, and 0.44 mGy/kBq for the kidney, PSMA+ PC3 PIP, and PSMA- PC3 flu tumors, respectively. When the activity concentration and distribution derived from the quantified  $\alpha$ -camera images were inserted in the nephron model for 1 MBq of  $^{211}\text{At}$ -6, an absorbed dose up to 123 Gy (or 123 mGy/kBq) in portions of the proximal tubules was determined. This is about 5-fold higher than the mean to the whole kidney and higher than glomerular doses (which were up to 42 Gy including self-dose and contribution from neighboring tubules). For the PSMA+ PC3

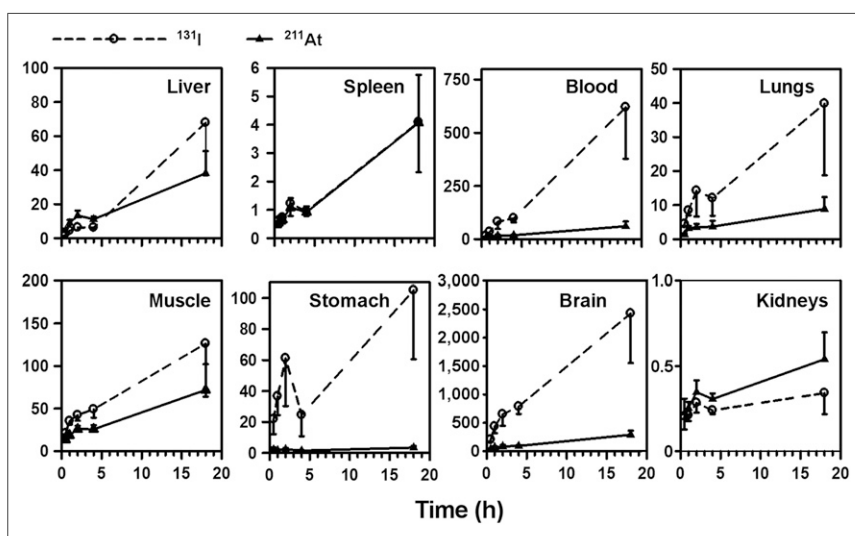


**FIGURE 4.** PSMA+ PC3 PIP tumor-to-tissue ratios after administration of 0.2 MBq of  $^{131}\text{I}$ -5 and  $^{211}\text{At}$ -6 in athymic mice. Values indicate mean  $\pm$  SD.

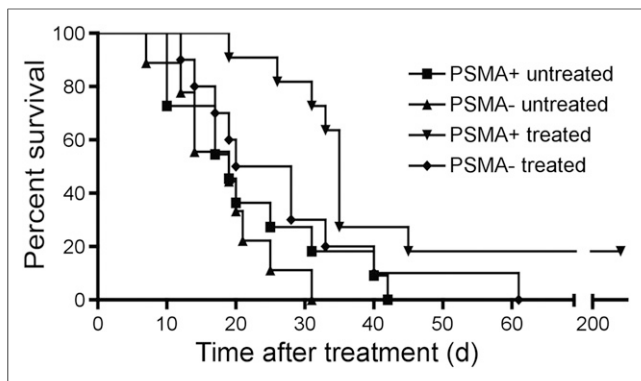


**FIGURE 5.**  $^{211}\text{At-6}$  showed significant tumor growth delay in flank xenograft model. Kaplan–Meier curve illustrating time for flank tumors to grow 10-fold in volume in athymic mice after 740 kBq of  $^{211}\text{At-6}$  treatment or control.

PIP tumor small-scale dosimetry, when the integrated activity and dose volume histograms were used, the dose per bin ranged from 0.26 to 36 Gy, for an average dose of 10 Gy and a root mean square of 5.5 Gy. The variability in uptake in the tumor gave an equivalent uniform dose of 6.9 Gy.

## DISCUSSION

We feature  $^{211}\text{At-6}$  in the context of a new paradigm for development of  $^{211}\text{At}$ -labeled small-molecule PSMA inhibitors for  $\alpha$ -RPT of PC. Treatment with  $^{211}\text{At-6}$  resulted in PSMA-specific cellular uptake and decreased clonogenic survival in vitro. This agent also offered significant tumor growth delay in a PSMA+ PC3 PIP flank xenograft model and significantly improved survival in a new PSMA+ micrometastatic PC model. Biodistribution studies showed uptake of  $^{211}\text{At-6}$  in PSMA+ PC3 PIP tumors and in kidneys. Microscale kidney dosimetry based on  $\alpha$ -camera images and a nephron model revealed hot spots in the proximal renal tubules, and long-term toxicity studies confirmed that the dose-limiting toxicity was late radiation nephropathy with loss of the proximal tubules.

The recent success of  $^{223}\text{RaCl}_2$ , which showed survival benefit and minimal toxicity in patients with CRPC, has demonstrated the feasibility of  $\alpha$ -particle RPT, but  $^{223}\text{RaCl}_2$  is limited to treatment of bone metastases.  $^{211}\text{At-6}$  is in a class of urea-based small molecules

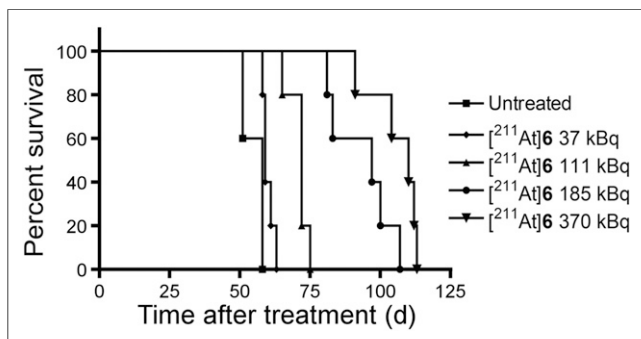


**FIGURE 6.**  $^{211}\text{At-6}$  showed significant improvement in survival in micrometastatic model. Kaplan–Meier curve shows survival time after treatment.

that targets PSMA and have shown uptake in pelvic and paraaortic lymph node metastases, prostate, visceral metastases, and bone metastases in human PC imaging studies (9,10). Accordingly, PSMA-targeted  $\alpha$ -particle RPT may be suitable for any PC site, particularly for micrometastatic disease not visible by imaging.  $\alpha$ -particles have potential advantages for treatment of micrometastatic cancer, including high linear energy transfer (100 keV/ $\mu\text{m}$  for  $^{211}\text{At}$ ) and short range (3–4 cells) versus  $\beta^-$ -emitters. Therefore, they may complement PSMA-targeted  $\beta^-$ -emitters such as  $^{131}\text{I}$ -MIP1466,  $^{177}\text{Lu}$ -labeled J591, and  $^{177}\text{Lu}$ -labeled PSMA imaging and therapy, under investigation for macroscopic disease (12,13,29). Previous studies have shown that the scaffold on which  $^{211}\text{At-6}$  was based has extremely high affinity for PSMA ( $K_i = 0.01$  nM) and that the targeted drug is localized not only to the plasma membrane but also to the perinuclear area of the cell, potentially increasing DNA damage (11). The potential for treatment of PC micrometastases with  $^{211}\text{At-6}$  is particularly supported by the improved survival demonstrated in our PSMA+ micrometastatic PC model (Fig. 6). This new model is a valuable tool for evaluation of PSMA-targeted therapy and imaging, with metastases developing in the liver, kidney, and bone after injection with PC3-ML-Luc-PSMA cells.

Although the potential for  $\alpha$ -particle RPT has been well established, clinical translation of these therapies has been challenging due to limited access to radionuclides, unresolved chemistry, in vivo instability, and need for improved dosimetry modeling. For  $^{211}\text{At}$ -labeled agents there is particular concern regarding dehalogenation in vivo. Our biodistribution results demonstrated mild uptake of  $^{211}\text{At}$  in the thyroid, stomach, spleen, and lungs, consistent with some deastatination (Fig. 4).

The short range of  $\alpha$ -particles may limit toxicity to off-target tissues, but for PSMA-targeted RPT there is concern regarding

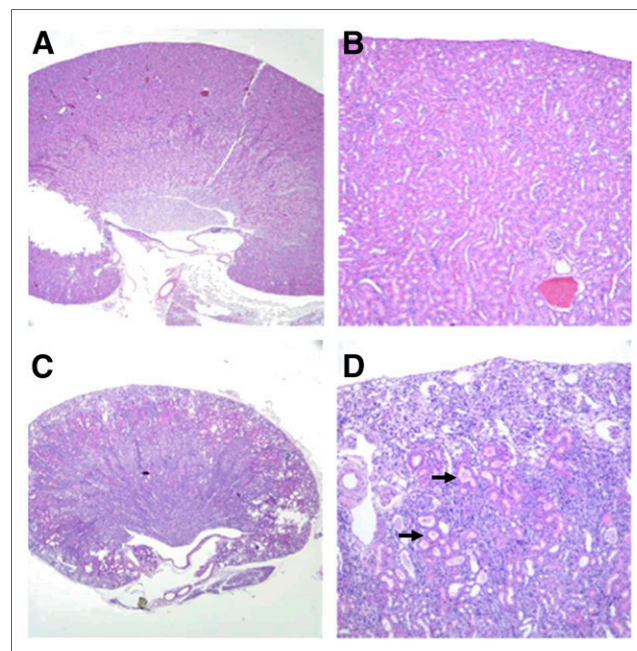


**FIGURE 7.** Renal histopathology from nontreated mouse (A and B) and mouse treated with 1.5 MBq of  $^{211}\text{At-6}$  (C and D). Treated kidney showed subcortical atrophy and degenerative loss of proximal tubules (arrows) consistent with late nephropathy due to  $\alpha$ -particle irradiation. A, C: 2 $\times$ ; B, D: 10 $\times$ .

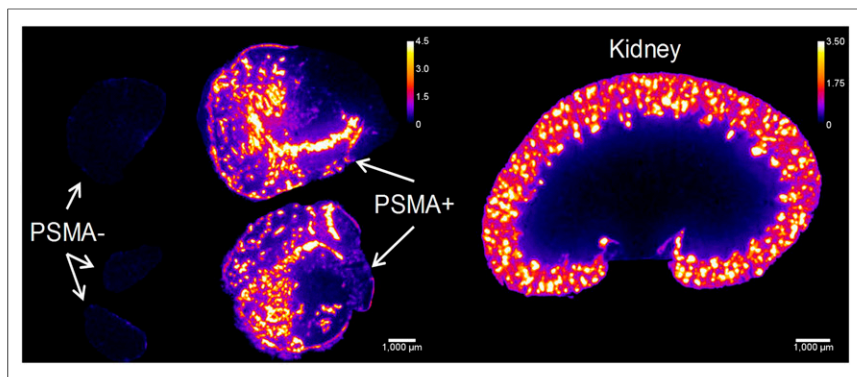


**FIGURE 8.**  $\alpha$ -camera images at 1 h showing relative  $^{211}\text{At-6}$  activity concentrations for PSMA+ and PSMA- tumors and kidneys. Scale shows activity concentration relative to whole tumor/ kidney average concentration. White bar = 1 mm.

renal toxicity due to physiologic PSMA expression in the proximal tubules. PSMA expression has been previously demonstrated in human proximal tubules by immunohistochemistry, and PSMA imaging in humans also demonstrates significant renal cortical uptake (6,29–31). Our study confirmed that the dose-limiting toxicity for  $^{211}\text{At-6}$  was late radiation nephropathy, demonstrated by both histopathology at necropsy and serial laboratory studies (Fig. 7). The maximum tolerated dose in CD1 mice was 37 kBq, and the lethal dose to 10% of mice was 111 kBq, which is lower than the lethal dose to 10% for  $^{211}\text{At-astatide}$  (555 kBq) in mice (32). Those toxicity results are consistent with the macro- and microlevel biodistribution and dosimetry modeling discussed below, emphasizing the importance of long-term toxicity studies and comprehensive dosimetry for characterization and translation of  $\alpha$ -particle RPT. To widen the therapeutic window for PSMA-targeted  $\alpha$ -particle RPT, we are currently investigating other urea-based agents with more favorable tumor-to-kidney dose ratios. Of note, our small-molecule  $^{211}\text{At-6}$  did not show significant acute hematologic toxicity, in contrast to high-molecular-weight RPTs such as antibodies that typically have dose-limiting hematologic toxicity.

$\alpha$ -camera images (Fig. 8) highlight the value of microscale dose calculations, particularly for short-range  $\alpha$ -emitters. Microscale dosimetry gave an absorbed dose to the critical substructure of the kidneys that was 5 times greater than the average whole kidney dose. The factor of 5 seems high given that the hot spot uptake is less than 5 at all time points. However, the model allows for a nontrivial empty lumen space that does not carry the activity; therefore, the dose can be greater in the model than a straightforward hot spot calculation. It is possible that with more sophisticated parameterization of the kidney, more accurate S values might be obtained. Concerning the distribution and shape of the hot spot activity, it is apparent that the hot spots do not cover the entire lengths of the tubules, which are convoluted and pass in and out of the tissue section planes. The likely explanation is that after passing through the glomeruli,  $^{211}\text{At-6}$  attaches to the nearest portion of the proximal tubule and does not span the full length of the tubules.

## CONCLUSION

PSMA-targeted  $\alpha$ -particle RPT with  $^{211}\text{At-6}$  resulted in specific PC cell kill in vitro and in vivo after systemic administration, showing promise for treatment of PC micrometastases. It also showed uptake in renal proximal tubules, resulting in late nephrotoxicity,

highlighting the importance of long-term toxicity studies and microscale dosimetry. Other agents are being developed with more favorable tumor-to-kidney dose ratios.

## DISCLOSURE

The costs of publication of this article were defrayed in part by the payment of page charges. Therefore, and solely to indicate this fact, this article is hereby marked “advertisement” in accordance with 18 USC section 1734. This work was supported by NIH CA116477, CA184228, CA134675, CA183031, CA157542, and EB005324 and in part by the Intramural Research Program of the NIH, National Cancer Institute, Center for Cancer Re-

search. No other potential conflict of interest relevant to this article was reported.

## ACKNOWLEDGMENTS

We thank Dr. Warren Heston for providing the PSMA+ PC3 PIP and PSMA- PC3 flu cells and Dr. Mauricio Reginato for the PC3-ML-Luc cells. We also acknowledge Dr. Tom Bäck (University of Gothenburg), who invented the alpha camera and collaborated on its installation and use in this study.

## REFERENCES

1. American Cancer Society. *Cancer Facts & Figures 2012*. Atlanta, GA: American Cancer Society; 2012.
2. Antonarakis ES, Feng Z, Trock BJ, et al. The natural history of metastatic progression in men with prostate-specific antigen recurrence after radical prostatectomy: long-term follow-up. *BJU Int*. 2012;109:32–39.
3. de Bono JS, Logothetis CJ, Molina A, et al. Abiraterone and increased survival in metastatic prostate cancer. *N Engl J Med*. 2011;364:1995–2005.
4. de Bono JS, Oudard S, Ozguroglu M, et al. Prednisone plus cabazitaxel or mitoxantrone for metastatic castration-resistant prostate cancer progressing after docetaxel treatment: a randomised open-label trial. *Lancet*. 2010;376:1147–1154.
5. Parker C, Nilsson S, Heinrich D, et al. Alpha emitter radium-223 and survival in metastatic prostate cancer. *N Engl J Med*. 2013;369:213–223.
6. Silver DA, Pellicer I, Fair WR, Heston WD, Cordon-Cardo C. Prostate-specific membrane antigen expression in normal and malignant human tissues. *Clin Cancer Res*. 1997;3:81–85.
7. Chang SS, O’Keefe DS, Bacich DJ, Reuter VE, Heston WD, Gaudin PB. Prostate-specific membrane antigen is produced in tumor-associated neovasculature. *Clin Cancer Res*. 1999;5:2674–2681.
8. Foss CA, Mease RC, Cho SY, Kim HJ, Pomper MG. GCPII imaging and cancer. *Curr Med Chem*. 2012;19:1346–1359.
9. Rowe SP, Macura KJ, Ciarallo A, et al. Comparison of prostate-specific membrane antigen-based  $^{18}\text{F}$ -DCFBC PET/CT to conventional imaging modalities for detection of hormone-naïve and castration-resistant metastatic prostate cancer. *J Nucl Med*. 2016;57:46–53.
10. Eiber M, Maurer T, Souvatzoglou M, et al. Evaluation of hybrid  $^{68}\text{Ga}$ -PSMA ligand PET/CT in 248 patients with biochemical recurrence after radical prostatectomy. *J Nucl Med*. 2015;56:668–674.
11. Kiess AP, Minn I, Chen Y, et al. Auger radiopharmaceutical therapy targeting prostate-specific membrane antigen. *J Nucl Med*. 2015;56:1401–1407.
12. Hillier S, Rubino K, Maresca K, et al. [ $^{131}\text{I}$ ]MIP-1466, a small molecule prostate-specific membrane antigen (PSMA) inhibitor for targeted radiotherapy of prostate cancer [abstract]. *J Nucl Med*. 2012;53(suppl 1):170.
13. Tagawa ST, Beltran H, Vallabhajosula S, et al. Anti-prostate-specific membrane antigen-based radioimmunotherapy for prostate cancer. *Cancer*. 2010;116(4, suppl):1075–1083.
14. Mulford DA, Scheinberg DA, Jurcic JG. The promise of targeted  $\alpha$ -particle therapy. *J Nucl Med*. 2005;46(suppl 1):199S–204S.
15. Larson SM, Carrasquillo JA, Cheung NK, Press OW. Radioimmunotherapy of human tumours. *Nat Rev Cancer*. 2015;15:347–360.

16. Guérard F, Gestin JF, Brechbiel MW. Production of [<sup>211</sup>At]-astatinated radiopharmaceuticals and applications in targeted  $\alpha$ -particle therapy. *Cancer Biother Radiopharm.* 2013;28:1–20.
17. Sgouros G., ed. *MIRD Monograph: Radiobiology and Dosimetry for Radiopharmaceutical Therapy with Alpha-Particle Emitters.* Reston, VA: Society of Nuclear Medicine and Molecular Imaging; 2016.
18. Chen Y, Foss CA, Byun Y, et al. Radiohalogenated prostate-specific membrane antigen (PSMA)-based ureas as imaging agents for prostate cancer. *J Med Chem.* 2008;51:7933–7943.
19. Maresca KP, Hillier SM, Femia FJ, et al. A series of halogenated heterodimeric inhibitors of prostate specific membrane antigen (PSMA) as radiolabeled probes for targeting prostate cancer. *J Med Chem.* 2009;52:347–357.
20. Banerjee SR, Foss CA, Castanares M, et al. Synthesis and evaluation of technetium-99m- and rhenium-labeled inhibitors of the prostate-specific membrane antigen (PSMA). *J Med Chem.* 2008;51:4504–4517.
21. Jackson PF, Cole DC, Slusher BS, et al. Design, synthesis, and biological activity of a potent inhibitor of the neuropeptidase N-acetylated alpha-linked acidic dipeptidase. *J Med Chem.* 1996;39:619–622.
22. Bhatnagar A, Wang Y, Mease RC, et al. AEG-1 promoter-mediated imaging of prostate cancer. *Cancer Res.* 2014;74:5772–5781.
23. Mukherjee A, Darlington T, Baldwin R, et al. Development and screening of a series of antibody-conjugated and silica-coated iron oxide nanoparticles for targeting the prostate-specific membrane antigen. *ChemMedChem.* 2014;9:1356–1360.
24. Bäck T, Jacobsson L. The alpha-camera: a quantitative digital autoradiography technique using a charge-coupled device for ex vivo high-resolution bioimaging of  $\alpha$ -particles. *J Nucl Med.* 2010;51:1616–1623.
25. Hobbs RF, Song H, Huso DL, Sundel MH, Sgouros G. A nephron-based model of the kidneys for macro-to-micro alpha-particle dosimetry. *Phys Med Biol.* 2012;57:4403–4424.
26. Vaidyanathan G, Affleck DJ, Zalutsky MR. Validation of 4-[fluorine-18]fluoro-3-iodobenzylguanidine as a positron-emitting analog of MIBG. *J Nucl Med.* 1995;36:644–650.
27. Pressman D, Day ED, Blau M. The use of paired labeling in the determination of tumor-localizing antibodies. *Cancer Res.* 1957;17:845–850.
28. Wilbur DS, Chyan MK, Hamlin DK, et al. Reagents for astatination of biomolecules: comparison of the in vivo distribution and stability of some radioiodinated/astatinated benzamidyl and nido-carboranyl compounds. *Bioconjug Chem.* 2004;15:203–223.
29. Weineisen M, Schottelius M, Simecek J, et al. <sup>68</sup>Ga- and <sup>177</sup>Lu-labeled PSMA I&T: optimization of a PSMA-targeted theranostic concept and first proof-of-concept human studies. *J Nucl Med.* 2015;56:1169–1176.
30. Kinoshita Y, Kuratsukuri K, Landas S, et al. Expression of prostate-specific membrane antigen in normal and malignant human tissues. *World J Surg.* 2006;30:628–636.
31. Cho SY, Gage KL, Mease RC, et al. Biodistribution, tumor detection, and radiation dosimetry of <sup>18</sup>F-DCFBC, a low-molecular-weight inhibitor of prostate-specific membrane antigen, in patients with metastatic prostate cancer. *J Nucl Med.* 2012;53:1883–1891.
32. McLendon RE, Archer GE, Garg PK, Bigner DD, Zalutsky MR. Radiotoxicity of systematically administered [<sup>211</sup>At]astatide in B6C3F1 and BALB/c (nu/nu) mice: a long-term survival study with histologic analysis. *Int J Radiat Oncol Biol Phys.* 1996;35:69–80.